Check for updates

Electron transfer dynamics and electrocatalytic oxygen evolution activities of the Co_3O_4 nanoparticles attached to indium tin oxide by self-assembled monolayers

Xuan Liu, Qianhong Tian, Yvpei Li, Zixiang Zhou, Jinlian Wang, Shuling Liu* and Chao Wang*

Shaanxi Collaborative Innovation Center of Industrial Auxiliary Chemistry and Technology, Department of Chemistry and Chemical Engineering, Key Laboratory of Auxiliary Chemistry and Technology for Chemical Industry, Ministry of Education, Shaanxi University of Science and Technology, Xi'an, Shaanxi, China

The Co_3O_4 nanoparticle-modified indium tin oxide-coated glass slide (ITO) electrodes are successfully prepared using dicarboxylic acid as the self-assembled monolayer through a surface esterification reaction. The ITO-SAM-Co_3O_4 (SAM = dicarboxylic acid) are active to electrochemically catalyze oxygen evolution reaction (OER) in acid. The most active assembly, with Co loading at 3.31×10^{-8} mol cm^{-2}, exhibits 374 mV onset overpotential and 497 mV overpotential to reach 1 mA cm^{-2} OER current in 0.1 M $HClO_4$. The electron transfer rate constant (k) is acquired using Laviron's approach, and the results show that k is not affected by the carbon chain lengths of the SAM (up to 18 -CH_2 groups) and that an increase in the average diameter of Co_3O_4 nanoparticles enhances the k. In addition, shorter carbon chains and smaller Co_3O_4 nanoparticles can increase the turn-over frequency (TOF) of Co sites toward OER. The Co_3O_4 nanoparticles tethered to the ITO surface show both a higher number of electrochemically active Co sites and a higher TOF of OER than the Co_3O_4 nanoparticles bound to ITO using Nafion.

Introduction

Electrodes with self-assembled monolayers (SAMs) have broad applications in the fields of sensing, catalysis, and energy storage and conversion. Understanding the electron transfer dynamics between the electrode substrate and the attached monolayer is crucial in designing interfaces for these applications (Kellon et al., 2019; Xie et al., 2019). Electrodes with tethered nanoparticles by the SAM feature low loadings and high atomic

utilization of nanoparticles, both of which are desirable in the field of catalysis (Young et al., 2016; Shermukhamedov et al., 2020; Lachmanová et al., 2021). Chazalviel and Allongue (2011) established a theory in describing the relationship between the insulating layer (SAM) thickness and electron transfer dynamics in the substrate-SAM-nanoparticle, where the electron transfer rate is unhindered until a threshold thickness of the SAM is reached. Later, Hill et al., 2015 proposed a model to qualitatively calculate the current of the substrate-SAM-nanoparticle assembly by considering the electron tunneling, reaction kinetics, and mass transport (Hill et al., 2015). Evidences supporting these theories using gold nanoparticles as the electron mediator are extensively reported (Wang et al., 2010; Barfidokht et al., 2013; Kizling et al., 2018; Liu et al., 2019). However, gold nanoparticles are catalytically inert in most cases, and nanoparticles with catalytic activities are desirable to be assembled onto the electrode surface in catalysis.

The main bottle-neck of hydrogen production by electrochemical water splitting is the anodic oxygen evolution reaction (OER, $2 H_2O \rightarrow 4 H^+ + O_2 + 4 e^-$, $E^o = 1.23$ V). The four coupled electron and proton transfer processes cause the sluggish kinetics of the OER, and active electrocatalysts and interfaces are required to reduce the large overpotential of the OER (Walter et al., 2010). The nanoparticle-attached electrodes have been constructed via SAM for OER. For example, iridium oxide nanoparticles (IrO_x) and ruthenium oxide nanoparticles (RuO_x) have been attached to the indium tin oxide-coated glass slide (ITO) surface *via* esterification reaction using polycarboxylic acids and pyrophosphoric acid as the linker, and the resulting electrodes are applied to catalyze the OER in acid (Gambardella et al., 2012; Tian et al., 2021). Consistent with the theory established by Chazalviel and Allongue (2011) the apparent electron transfer rates of the IrO_x-modified electrodes are unhindered using the linkers with short carbon-chains, and the electron tunneling rate does not limit the OER rate (Gambardella et al., 2012; Tian et al., 2021). Since iridium is a precious metal, interfaces with nonprecious metal nanoparticles are highly desirable to catalyze the OER. Spinel-type cobalt oxide nanoparticles (Co_3O_4) have been adopted to catalyze the OER in acid and are a promising candidate in replacing in part the precious metal catalysts (Lai et al., 2021; Natarajan et al., 2021). Co_3O_4 is usually electrodeposited on the substrate surface or is bonded to the substrate surface using Nafion (Liu et al., 2013). These methods inevitably lead to low percentage of utilization of electrochemically active Co atoms as the active sites, as some nanoparticles are not in direct contact with the electrolyte. The substrate-SAM-Co_3O_4 assembly offers a promising route in fine-tuning the surface structure of the catalytic active surface, with a maximum percentage of Co exposed. Therefore, we report the construction of the ITO-SAM-Co_3O_4 (SAM = dicarboxylic acid) assembly, and the constructed interface is active toward the OER in acid. The influences of SAM chain lengths and the average diameters of the Co_3O_4 on the electron transfer kinetics and on

the electrocatalytic OER activities are investigated. Also, comparisons to the electrode with Nafion-bound Co_3O_4 are made, and the Co_3O_4 tethered by SAM show significantly enhanced number of electrochemically active Co sites and increased OER activity per active site.

Experimental section

Preparation of Co_3O_4

Chemicals used are listed in the Supplementary Information. The surfactant-free Co_3O_4 were synthesized based on the literature report (Dong et al., 2007). The procedure to prepare Co_3O_4 with an average diameter of 3.5 nm is as follows. The 0.5 g cobalt (II) acetate tetrahydrate ($Co(ac)_2$ 4 H_2O) was dissolved in 25 ml ethanol, and 2.5 ml 25% $NH_3 \cdot H_2O$ was added under vigorous stirring. The solution was stirred for 10 min in air and was transferred into a Teflon-lined stainless-steel. The autoclave was kept at 150°C for 3 h. The colloidal solution was centrifuged at 10,000 rpm for 15 min to acquire the Co_3O_4 precipitates. The precipitates were washed twice with distilled water and dried in the oven at 60°C for 4 h. The Co_3O_4 with various sizes were synthesized following the same procedure, but different amounts of the reactants ($Co(ac)_2$ 4 H_2O, C_2H_5OH, H_2O, and $NH_3 \cdot H_2O$) were added according to Supplementary Table S1. The XRD and TEM images of the as-synthesized Co_3O_4 with various sizes are shown in the Supplementary Information (Supplementary Figures S1, S3).

Preparation of the ITO-SAM-Co_3O_4

The ITO was cleaned with water and ethanol under sonication and was dried. Then, the ITO was immersed in 5 ml of acetone containing dicarboxylic acid (glutaric acid, 1,8-octanedioic acid, 1,16-hexadecanedioic acid, or 1,20-eicosanedioic acid) for 3 h to allow the adsorption of the acid onto the ITO surface. The ITO-SAM (ITO-Glu, ITO-Oct, ITO-Hex, or ITO-Eic) was washed with acetone and dried in air. The acid-adsorbed ITO was immersed in the 5 ml colloidal solution (pH adjusted to 2.0 using HCl) containing 3.5 nm Co_3O_4 (4.6 mg ml^{-1}) for 4 h. After being taken out from the solution, the ITO-SAM-Co_3O_4 was washed with 0.1 M $HClO_4$. Electrodes prepared using glutaric acid, 1,8-octanedioic acid, 1,16-hexadecanedioic acid, and 1,20-eicosanedioic acid are labeled as ITO-Glu-Co_3O_4, ITO-Oct-Co_3O_4, ITO-Hex-Co_3O_4, and ITO-Eic-Co_3O_4, respectively. The concentrations of the carboxylic acids in acetone are listed in Supplementary Table S2 in the Supplementary Information. Surface loadings of Co are checked by ICP-AES and are in the range of $2.0–5.5 \times 10^{-8}$ mol cm^{-2}.

To prepare ITO-Oct-Co_3O_4 with different sizes of Co_3O_4 attached, the ITO-Oct was immersed in a 5 ml colloidal solution

SCHEME 1
Procedure to prepare ITO-SAM-Co$_3$O$_4$ (SAM = dicarboxylic acid).
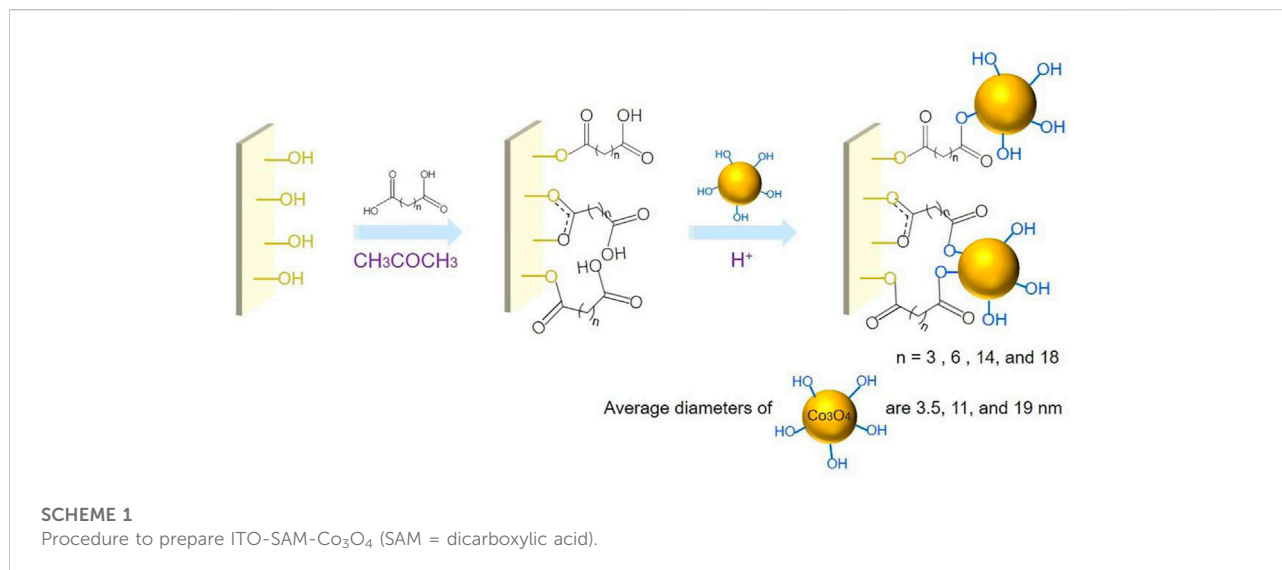
(pH 2.0) containing Co$_3$O$_4$ with different sizes for 4 h. Electrodes prepared using Co$_3$O$_4$ with average diameters of 11 and 19 nm are labeled as ITO-Oct-Co$_3$O$_4$ (11) and (19), respectively. The ITO-Co$_3$O$_4$ was prepared by directly immersing a bare ITO into a Co$_3$O$_4$ colloidal solution for 4 h, and the ITO-Oct-CoCl$_2$ was fabricated by immersing the ITO-Oct in a 5 ml 0.0016 M CoCl$_2$ aqueous solution.

Preparation of the Co$_3$O$_4$/Nafion electrode

The ink was prepared by dispersing 0.0011 g Co$_3$O$_4$ with 3.5 nm average diameter into 20 ml of absolute ethanol, with 30 μl of 0.5% Nafion added. After sonication for 30 min, 50 μl of the solution was drop-coated on the ITO surface with ~1 cm^2 covered. After being dried in air, the Co$_3$O$_4$/Nafion electrode is used for electrochemical tests. The loading of the Co on the ITO-Oct-Co$_3$O$_4$ and Co$_3$O$_4$/Nafion electrodes is the same (3.31 × 10^{-8} mol cm^{-2}).

Electrochemical method

The CHI660E and ParSTAT MC potentiostats are used to carry out the electrochemical tests in the three-electrode system. A saturated calomel electrode (SCE) is used as the reference and a polished graphite rod as the counter. The geometric surface area of the working electrode in the electrolyte is controlled to 1 cm^2. All potentials reported are relative to the reversible hydrogen electrode. The linear sweep voltammograms (LSVs) are corrected for the solution resistance. Other information about the instrumentation is provided in the Supplementary Information.

Results and discussion

Scheme 1 illustrates the procedure to fabricate the ITO-SAM-Co$_3$O$_4$ (SAM = dicarboxylic acid). In acetone solution containing the dicarboxylic acid, surface hydroxyl groups of ITO can react with the carboxylic acid groups to form ester bonds. Then, the ITO-SAM (SAM = dicarboxylic acid) is immersed in the acidic solution containing Co$_3$O$_4$ to allow the esterification between the adsorbed carboxylic acid groups and the hydroxyl groups of Co$_3$O$_4$. Hydroxyl groups on the Co$_3$O$_4$ surface have been observed previously (Anantharaj et al., 2019), and the interaction of carboxylic acid groups with the Co$_3$O$_4$ surface hydroxyl groups has also been reported (Kollhoff et al., 2018). Dicarboxylic acids with different numbers of carbon chains are adopted. The Co$_3$O$_4$ with various average diameters (3.5, 11, and 19 nm) are synthesized, and the TEM (Supplementary Figure S3) and XRD (Supplementary Figure S1) of the Co$_3$O$_4$ powders are shown in the Supplementary Information. All XRD patterns show diffraction peaks that correspond to the face-centered cubic phase of Co$_3$O$_4$ (JCPDS 09-0418) (Dong et al., 2007), and Co$_3$O$_4$ with larger average diameters show increased XRD peak intensities, which suggests their better crystallinities. The pH of the Co$_3$O$_4$-containing solution (pH = 2.0) is lower than the pKa$_1$ values of the polycarboxylic acids adopted [glutaric acid 4.34 (Canari and Eyal, 2003), 1,8-octanedioic acid 4.5 (Hullar and Anastasio, 2011), 1,16-hexadecanedioic acid 4.65 (Kanicky and Shah, 2002), and 1,20-eicosanedioic acid 5.5 (Mukerjee and Ostrow, 2010)]; therefore, carboxylic acid groups remain in the -COOH form to allow the esterification reaction to happen.

We first used cyclic voltammetry (CV) to probe the surface change during the fabrication of the ITO-Oct-Co$_3$O$_4$. Figure 1 shows the results. For the ITO-Oct-Co$_3$O$_4$, a couple of redox peaks are shown at ~ 1.58 V, which can be assigned to the Co$^{3+/4+}$
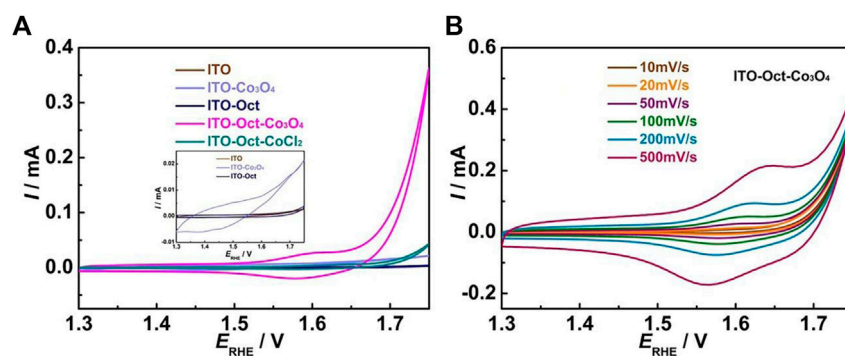
FIGURE 1
(A) CV of the bare ITO, ITO-Oct, ITO-Co₃O₄, ITO-Oct-Co₃O₄, and ITO-Oct-CoCl₂ at 50 mV s⁻¹ in 0.1 M HClO₄; **(B)** CV of the ITO-Oct-Co₃O₄ at various scan rates (10−500 mV s⁻¹) in 0.1 M HClO₄.
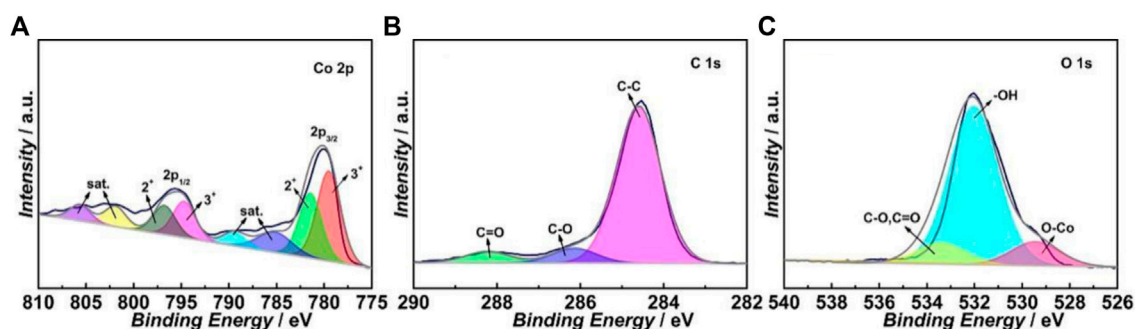

FIGURE 2
Deconvoluted high-resolution XPS spectra of the **(A)** Co 2p, **(B)** C 1s, and **(C)** O 1s regions of the ITO-Oct-Co₃O₄.

redox couple in acid (Xiao et al., 2020; Han et al., 2021; Natarajan et al., 2021). The charge under the anodic $Co^{3+/4+}$ peak is integrated, and the number of electrochemically active Co atoms (Γ) is estimated to be 4.6×10^{-10} mol cm^{-2} based on the integrated charge, assuming a $1\,e^-$ transfer process. The total amount of Co on the ITO-Oct-Co₃O₄ is 3.31×10^{-8} mol cm^{-2} acquired using ICP-AES. These values indicate that 1.4% of the Co on the electrode is electrochemically active. Starting at 1.65 V, the OER process happens. In comparison, the CV of the bare ITO and ITO-Oct is identical (Figure 1A inset) and lack the characteristic $Co^{3+/4+}$ redox peaks and the OER process. Electrodes prepared by simply immersing the ITO into the Co₃O₄ colloidal solution (ITO-Co₃O₄) give rise to a higher CV current than bare ITO and show redox features, but the current is still negligible compared to the ITO-Oct-Co₃O₄. We also observed a strong dependence of the coverage of the Co₃O₄ on the pH of the esterification reaction (Supplementary Figure S4), which implies that the ester bonds formed are the major driving force to anchor the Co₃O₄ to the surface, while the ionic

interaction, hydrogen bonding, and chelation between the acid and the defected cationic centers contribute insignificantly to the surface bonding as they are less dependent on pH. Immersing the ITO-Oct in CoCl₂ solution (ITO-Oct-CoCl₂) leads to formation of Co^{2+} coordinated to the carboxylic acid groups at the surface, and the CV lacks the unique feature for $Co^{3+/4+}$ redox couple but shows a slight increase in the OER current at high potentials. These show that the Co₃O₄, rather than Co ionic species, are tethered to the ITO in case of the ITO-Oct-Co₃O₄. Figure 1B displays the CV of the ITO-Oct-Co₃O₄ at various scan rates in 0.1 M HClO₄. All the CV show distinct $Co^{3+/4+}$ redox peaks, and by plotting the log i_p versus log v (Supplementary Figure S5), the slope is close to 1, which implies that the redox active species are confined to the electrode surface (Silva et al., 2014).

Figure 2A shows the deconvoluted XPS spectrum of the Co 2p region of the ITO-Oct-Co₃O₄. The Co $2p_{3/2}$ peak can be deconvoluted into two components at 781.5 and 779.5 eV, which originate from the Co^{2+} and Co^{3+} in the Co₃O₄, respectively (Zhang et al., 2018). The deconvoluted Co $2p_{1/2}$
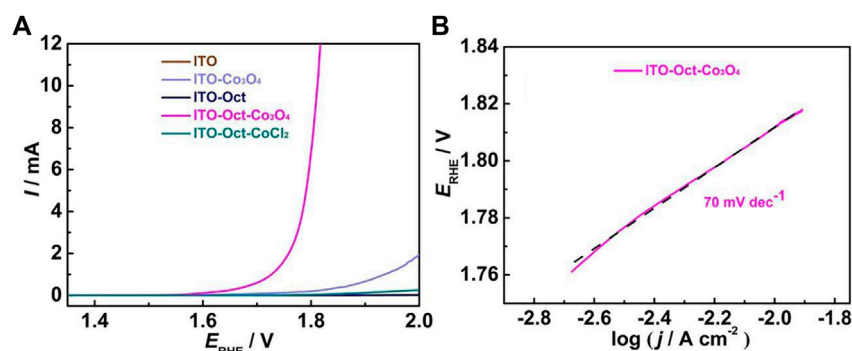
FIGURE 3
(A) LSV of the bare ITO, ITO-Oct, ITO-Co_3O_4, ITO-Oct-Co_3O_4, and ITO-Oct-$CoCl_2$ at 5 mV s^{-1} in 0.1 M HClO$_4$; **(B)** Tafel plot of the ITO-Oct-Co_3O_4.

TABLE 1 Summary of the key electrochemical parameters of the ITO-SAM-Co_3O_4 (SAM = dicarboxylic acid).

	SAM	Γ_{cv}/ nmol cm^{-2}	η_{onset}/ mV	η@ 1 mA cm^{-2}/mV	η@ 5 mA cm^{-2}/mV	Tafel Slope/mV dec^{-1}	TOF@ 1.72 V/s^{-1}	k/s^{-1}
ITO-Glu-Co_3O_4	HOOC(CH$_2$)$_3$COOH	0.39	433 ± 1	514 ± 1	597 ± 4	98	3.87 ± 0.03	1.12 ± 0.07
ITO-Oct-Co_3O_4	HOOC(CH$_2$)$_6$COOH	0.46	374 ± 4	497 ± 2	562 ± 3	70	4.06 ± 0.04	1.11 ± 0.04
ITO-Hex-Co_3O_4	HOOC(CH$_2$)$_{14}$COOH	0.55	402 ± 1	514 ± 1	590 ± 4	109	2.70 ± 0.01	1.10 ± 0.02
ITO-Eic-Co_3O_4	HOOC(CH$_2$)$_{18}$COOH	0.32	444 ± 1	529 ± 1	598 ± 6	91	2.87 ± 0.01	1.14 ± 0.08
ITO-Oct-Co_3O_4 (11)	HOOC(CH$_2$)$_6$COOH	0.33	449 ± 2	525 ± 1	590 ± 3	112	3.02 ± 0.07	1.15 ± 0.09
ITO-Oct-Co_3O_4 (19)	HOOC(CH$_2$)$_6$COOH	0.33	451 ± 1	533 ± 1	623 ± 2	84	2.88 ± 0.04	1.35 ± 0.07

peak also shows the contribution from the Co^{2+} (796.8 eV) and Co^{3+} (794.7 eV) components. The deconvoluted C 1s spectrum in Figure 2B displays three peaks at 284.6, 286.1, and 288.2 eV, which correspond to the C-C, C-O, and C=O bonds, respectively (Dwivedi et al., 2015). The deconvoluted O 1s peak in Figure 2C shows three components at 529.4, 532.0, and 533.4 eV, which match the Co-O bond in the Co_3O_4, surface -OH structure, and the C-O and C=O bonds, respectively (Yang et al., 2009). The existence of C=O and C-O structures in both C 1s and O 1s spectra indicates the formation of ester bonds. The XRD pattern of the ITO-Oct-Co_3O_4 shows only crystalline peaks assigned to the ITO substrate (Supplementary Figure S2), suggesting the loading of crystalline Co_3O_4 is low. Both the XPS and CV show that the Co_3O_4 are successfully tethered to the ITO surface using the dicarboxylic acid as SAM.

Figure 3A compares the OER activity of the ITO-Oct-Co_3O_4 with bare ITO, ITO-Oct, ITO-Co_3O_4, and ITO-Oct-$CoCl_2$ in

0.1 M HClO$_4$ at 5 mV s^{-1}. Significantly higher OER current is observed at the high-potential region (>1.65 V) for the ITO-Oct-Co_3O_4, while the ITO and ITO-Oct exhibit negligible current in the similar region. This indicates that the attached Co_3O_4 is responsible for the observed OER activity. The OER onset overpotential of the ITO-Oct-Co_3O_4 is 374 mV, and the overpotential to reach 1, 5, and 10 mA cm^{-2} current densities is 497, 562, and 570 mV, respectively. The Tafel plot and the corresponding Tafel slope value of the ITO-Oct-Co_3O_4 are displayed in Figure 3B. The Tafel slope value acquired is 70 mV dec^{-1}, consistent with the reported Tafel slopes of Co_3O_4 in acid (Mondschein et al., 2017; Han et al., 2021). The turn-over frequency (TOF) at 1.72 V is calculated based on Eq. 1

$$\text{TOF} = j/4F\Gamma \qquad (1)$$

to be 4.06 s^{-1}. The key electrochemical parameters of the ITO-Oct-Co_3O_4 are summarized in Table 1.
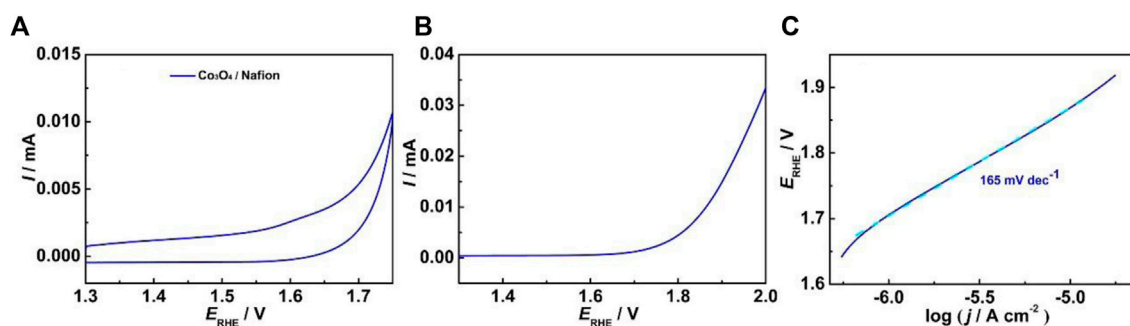
FIGURE 4
(A) CV of the Co_3O_4 bound by Nafion on ITO at 50 mV s^{-1} in 0.1 M HClO$_4$; **(B)** LSV of the electrode at 5 mV s^{-1} in 0.1 M HClO$_4$; **(C)** Tafel plot of the electrode.

We also prepared the Co_3O_4 (3.5 nm in average diameter bound by Nafion on ITO, and the amount of Co deposited on the ITO is controlled to 3.31×10^{-8} mol cm^{-2}, same as the ITO-Oct-Co_3O_4. Figure 4A shows the CV of the electrode at 50 mV s^{-1} in 0.1 M HClO$_4$. Weak $Co^{3+/4+}$ redox peaks are shown centered at 1.63 V. By integrating the charge under the $Co^{3+/4+}$ anodic peak of the Co_3O_4/Nafion electrode, assuming a 1 e$^-$ transfer process, the Γ is estimated to be 6.66×10^{-11} mol cm^{-2}. This indicates that the ITO-Oct-Co_3O_4 exposes seven times higher amount of the electrochemically active Co atoms than the Co_3O_4/Nafion electrode with the same Co_3O_4 loading. This is consistent with previous observations using IrO$_x$ and Au nanoparticles and can be caused by the inhomogeneous distribution of Nafion bound Co_3O_4 at the ITO surface, as aggregation is constantly observed on the Nafion bound nanoparticles (Moghaddam et al., 2015). In addition, different substrate–nanoparticle interactions and parallel interactions can account for the observed differences in the Γ. Figure 4B shows the LSV of the Co_3O_4/Nafion electrode. The OER process is also observed starting ~480 mV overpotential, but the OER current at 1.72 V is significantly lower than that of the ITO-Oct-Co_3O_4, in part attributed to the lower Γ. The TOF at 1.72 V for the Co_3O_4/Nafion electrode is calculated to be 0.058 s^{-1}, 69 times lower than that of the ITO-Oct-Co_3O_4. Figure 4C shows the Tafel plot of the Co_3O_4/Nafion electrode. The Tafel slope value of the Co_3O_4/Nafion electrode is 165 mV dec^{-1}. This suggests sluggish OER kinetics of the Co_3O_4/Nafion electrode. Both the lower TOF and the higher Tafel slope value for the Co_3O_4/Nafion electrode indicate inferior electrocatalytic activity per active Co site for the electrode with Nafion-bound Co_3O_4. As we adopted the same Co_3O_4, the surface structure of the active sites is similar. The observed inferior activity per active Co site is probably caused by the hindered electron or proton transport for the OER process. This proposal agrees with the results acquired by Young et al. (2016), where molecular tether facilitates the Au nanoparticle-mediated electron transfer process (Young et al., 2016).

Therefore, the dicarboxylic acid-tethered Co_3O_4 exposed significantly higher amount of electrochemically active Co atoms than the Nafion bound Co_3O_4, and the electrocatalytic OER activities of nanoparticles acquired using the Nafion as the binder can be a severe underestimation.

The surface modification process is further conducted using carboxylic acids with different chain lengths. Figure 5 A–C shows the CV at various scan rates of the ITO-Glu-Co_3O_4, ITO-Hex-Co_3O_4, and ITO-Eic-Co_3O_4, respectively, in 0.1 M HClO$_4$. All electrodes show distinct $Co^{3+/4+}$ redox peaks, which suggests the successful attachment of the Co_3O_4 to ITO. The CV at 50 mV s^{-1} was used to estimate the Γ, and the results are summarized in Table 1. Figure 5D displays the LSV for the ITO-Glu-Co_3O_4, ITO-Hex-Co_3O_4, and ITO-Eic-Co_3O_4 from 1.3–1.9 V at 10 mV s^{-1}. All electrodes display electrocatalytic OER activities that originate from the Co_3O_4. The corresponding Tafel plots are shown in Figure 5E, and similar Tafel slope values for all three electrodes are observed, which suggests similar OER mechanistic pathways. The Tafel slope values, overpotentials at 1 and 5 mA cm^{-2}, and the TOF at 1.72 V of these electrodes are summarized in Table 1. The electron transfer rate constants (k) are analyzed using the peak separations from CV at various scan rates based on Laviron's approach (Lavagnini et al., 2004; Lachmanová et al., 2021). The $E_{peak} - E^{0'}$ is related to ln ν by Eq. 2,

$$E_{peak} - E^{0'} = -\frac{RT}{\alpha nF} \ln\left(\frac{\alpha nF\nu}{RTk}\right), \qquad (2)$$

where E_{peak} is the redox peak potential, $E^{0'}$ is the formal redox potential, α is the transfer coefficient, n is the number of electrons transferred, and other symbols have their standard meanings. By plotting the $E_{peak} - E^{0'}$ against the ln ν, the fitted line intercepts with the x-axis, and the k can be calculated based on Eq. 3.
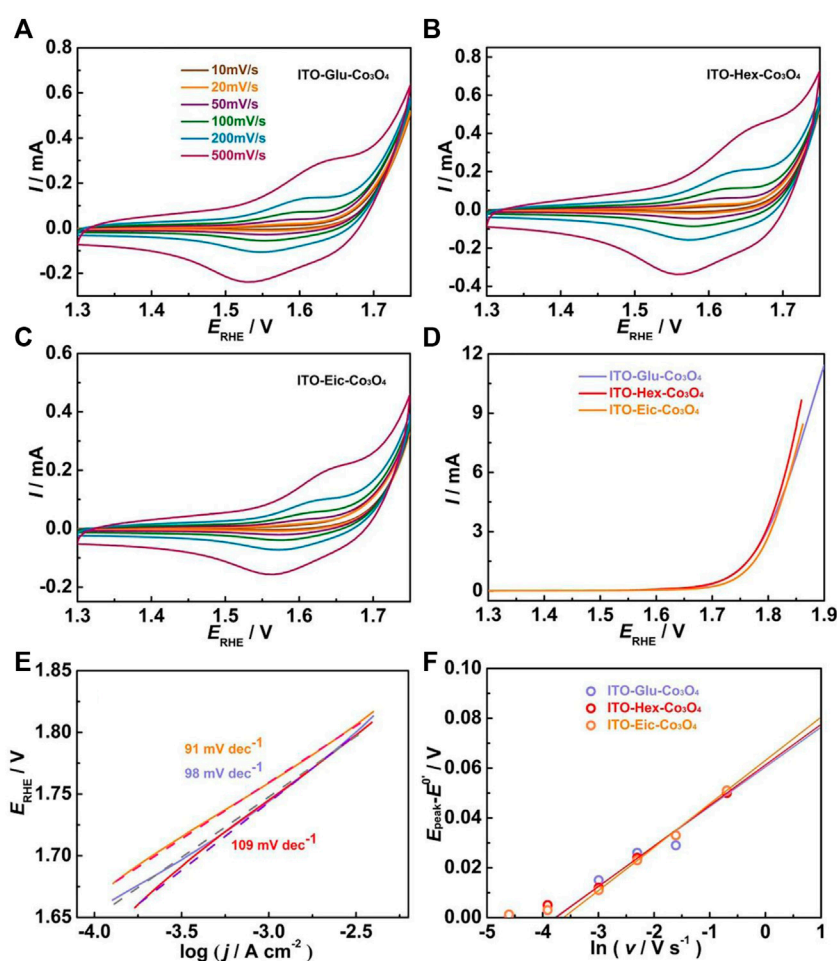
$$k = \frac{\alpha nF\nu}{RT}. \qquad (3)$$

FIGURE 5
(A–C) CV of the ITO-Glu-Co₃O₄, ITO-Hex-Co₃O₄, and ITO-Eic-Co₃O₄ at various scan rates in 0.1 M HClO₄; **(D)** LSV of these electrodes at 5 mV s⁻¹ in 0.1 M HClO₄; **(E)** Corresponding Tafel plots and the Tafel slope values of these electrodes; **(F)** Plots of anodic (E_{peak}–E^0) against ln v of these electrodes.

Figure 5F shows the E_{peak}–$E^{0'}$ versus ln v plot for the ITO-Glu-Co₃O₄, ITO-Hex-Co₃O₄, and ITO-Eic-Co₃O₄. The calculated k values are close and are summarized in Table 1.

By utilizing Co₃O₄ with different average diameters, ITO-Oct-Co₃O₄ (11) and (19) are constructed. Figures 6A,B display the CV at various scan rates in 0.1 M HClO₄ for the ITO-Oct-Co₃O₄ (11) and (19), respectively. Both electrodes show Co³⁺/⁴⁺ redox peaks, and the Γ are calculated and summarized in Table 1. Figure 6C shows the LSV of these electrodes. Both electrodes are active toward OER, and the OER onset overpotential and overpotentials to reach 1 and 5 mA cm⁻² and the TOF at 1.72 V are all summarized in Table 1. Figure 6D shows the Tafel slope of these two electrodes. The Tafel slope values for the ITO-Oct-Co₃O₄ (11) and (19) are 112 and 84 mV dec⁻¹, respectively. Figure 6E shows the E_{peak}–$E^{0'}$ versus ln v plots for the ITO-Oct-Co₃O₄ (11) and (19), together with the ITO-

Oct-Co₃O₄ (the one with 3.5 nm average diameter. The calculated k values are summarized in Figure 6F and in Table 1.

From Table 1, we observe a dependence of k on the nanoparticle size, as k increases with the increased average diameter of the Co₃O₄. Based on the Marcus theory of electron transfer, the k is related to the reorganization energy (λ) and the extent of electron coupling. For an NP with a radius r, the λ is related to nanoparticle radius (r) by Eq. 4 (Chazalviel and Allongue, 2011),

$$\lambda = \frac{q^2}{4\pi\varepsilon_0 r},\qquad(4)$$

where q is the unit charge and ε_0 is the vacuum permittivity. A larger r of the nanoparticle would entail a lower λ, which increases the rate of electron transfer. The dependence of k on the carboxylic acid chain lengths is not obvious as all k of the
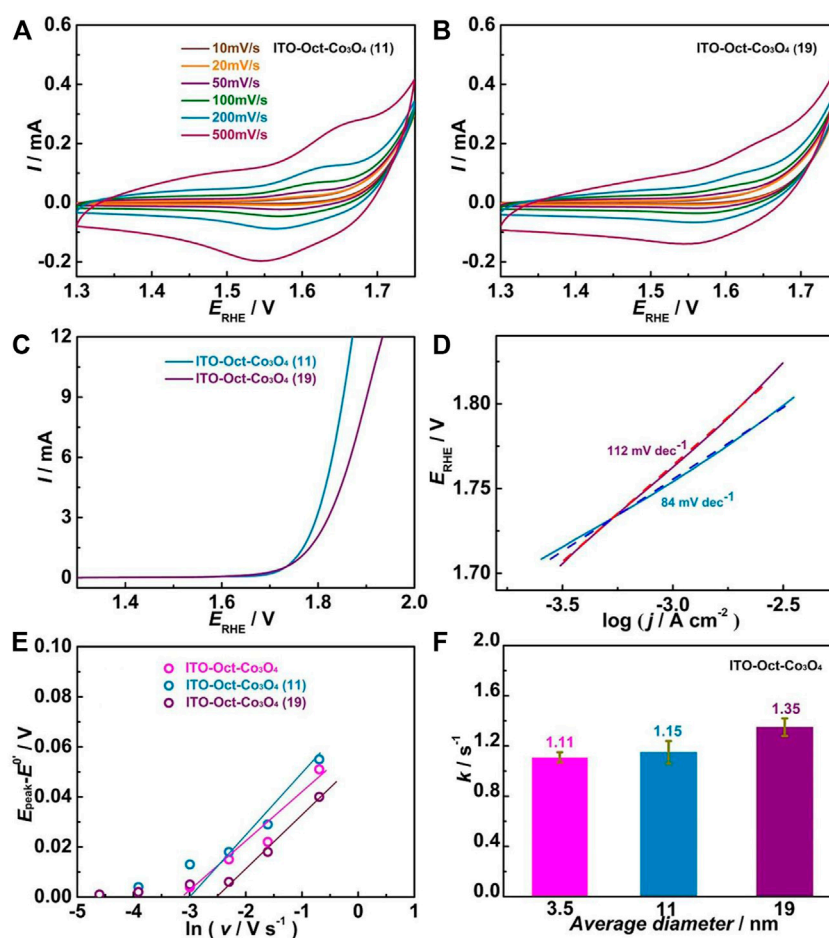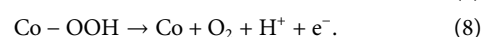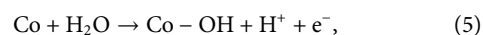
FIGURE 6
(A,B) CV of the ITO-Oct-Co$_3$O$_4$ (11) and (19) at various scan rates in 0.1 M HClO$_4$; **(C)** LSV of these electrodes at 5 mV s^{-1} in 0.1 M HClO$_4$; **(D)** Corresponding Tafel plots of these electrodes; **(E)** Plots of anodic (E_{peak}–E^0) against ln v of these electrodes; **(F)** k versus the average diameter of Co$_3$O$_4$ of the ITO-Oct-Co$_3$O$_4$.

ITO-Glu-Co$_3$O$_4$, ITO-Oct-Co$_3$O$_4$, ITO-Hex-Co$_3$O$_4$, and ITO-Eic-Co$_3$O$_4$ are in the range of 1.10–1.14 s^{-1}. This phenomenon is consistent with Chazalviel's theory describing the relationship between the insulating layer thickness and the k in the substrate–SAM–nanoparticle assembly (Chazalviel and Allongue, 2011). Based on their theory, nanoparticles with 3.5 nm in diameter in the substrate–SAM–nanoparticle assembly would require approximately 20 –CH$_2$- units in the carbon chain to reach the critical point, above which electron transfer would become hindered. In our case, no hindered electron transfer is observed using carboxylic acids with 18 or fewer –CH$_2$- units. Also, this observation is in accordance with Bard's model where the tunneling current, though it decreases with increased distance between the substrate surface and the nanoparticle, is still higher than the kinetic current of the Co$^{3+/4+}$ oxidation process. The k values reported are close to the literature value where Wang et al. fabricated the electrodeposited Co$_3$O$_4$

nanosheet on Ti foil in 1 M KOH and observed the k at 0.29 s^{-1} (Xiao et al., 2020).

The electrocatalytic OER mechanism of Co$_3$O$_4$ is proposed through four consecutive proton-coupled electron transfer (PCET) processes in acid as shown in Eqs 5–8 (Shinagawa et al., 2015; Srinivasa et al., 2020; Xiao et al., 2020).

$$Co + H_2O \rightarrow Co - OH + H^+ + e^-, \quad (5)$$
$$Co - OH \rightarrow Co - O + H^+ + e^-, \quad (6)$$
$$Co - O + H_2O \rightarrow Co - OOH + H^+ + e^-, \quad (7)$$
$$Co - OOH \rightarrow Co + O_2 + H^+ + e^-. \quad (8)$$

where Co represents an electrochemically active Co site and the –O, –OH, and –OOH represent the surfaced-adsorbed oxo, hydroxyl, and peroxyl intermediates, respectively. The Tafel slope at 120 mV dec^{-1} represents that the adsorption of -OH is rate-limiting (Eq. 5), while the Tafel slope of 40 mV

dec^{-1} suggests that the deprotonation of –OH to form –O is rate-limiting (Eq. 6). Tafel slopes between these two values arise owing to different relative rates of the first two elementary steps in the mechanism. On the Co_3O_4 surface, the Tafel slope of our electrodes and literature reported values all lie in the range of 79–120 mV dec^{-1}, which suggests that the adsorption of –OH is rate-limiting (Mondschein et al., 2017; Han et al., 2021; Natarajan et al., 2021). This is also consistent with the volcano plots calculated by DFT (Song et al., 2020). Other interpretations of the Tafel slope include the influence of the dissolution of Co_3O_4 during the OER that leads to a Tafel slope value that deviates from the typical one (Mondschein et al., 2017).

The TOF of the ITO-SAM-Co_3O_4 depends on the carbon chain length of the dicarboxylic acid, with the ITO-Glu-Co_3O_4 and the ITO-Oct-Co_3O_4 being higher than the ITO-Hex-Co_3O_4 and the ITO-Eic-Co_3O_4. This might be caused by the decrease of the tunneling current with increased chain lengths of the SAM, which entails the shift from the OER kinetics-controlled current to the mixed tunneling and OER kinetics-controlled current according to Bard's model. Also, a decrease in the TOF is observed with larger Co_3O_4 size. This suggests that the OER activity per active Co site is lower in the case of larger nanoparticles, which is related to the structure of Co_3O_4, like crystallinity and surface defects. The OER activity of the constructed ITO-Oct-Co_3O_4 is compared to that of other reported Co_3O_4 electrocatalysts in acid, and the results are summarized in Supplementary Table S3. However, the stability of the constructed ITO-Oct-Co_3O_4 is limited toward OER in acid, which is mainly attributed to the dissolution of active Co sites from Co_3O_4 as evidenced by the loss of Co features in CV during repetitive potential cycling (Supplementary Figure S6). ICP-AES on the electrolyte after 1,000 cycles of the potential cycling shows that 13% of Co was leached into the electrolyte. Also, the ITO-Oct-Co_3O_4 can only sustain the 0.05 mA cm^{-2} galvanostatic measurement for 2500 s in 0.1 M $HClO_4$ (Supplementary Figure S8). In acid, the gradual formation of a porous hydrous oxide layer with a loosely bonded Co center is observed and is proposed to be related to OER stability (Natarajan et al., 2021). The formed hydrous oxide layers could also affect the stability of the anchoring ester groups, which could lead to loss of the Co_3O_4. Further optimization of the Co_3O_4 structure, like the incorporation of acid stable components (Huynh et al., 2017), is required to enhance the stability of the assembly.

Conclusion

We constructed the Co_3O_4-modified ITO electrodes using dicarboxylic acid as the bridging molecule. The ITO-SAM-Co_3O_4 were characterized using electrochemistry and XPS and are active toward the OER in acid. The ITO-Oct-Co_3O_4, with Co loading at 3.31×10^{-8} mol cm^{-2} exhibits 374 mV onset overpotential and 497 mV overpotential to reach 1 mA cm^{-2} OER current density in 0.1 M $HClO_4$. The k is not affected by the carbon chain lengths of the SAM, and an increase in the Co_3O_4 size enhances the k, which is consistent with the previous theory of the electron transfer kinetics. Enhanced TOF of the OER is observed on electrodes with shorter carbon chains and smaller Co_3O_4. Meanwhile, the stability of the ITO-SAM-Co_3O_4 is limited by the Co_3O_4, which is prone to dissolute under the OER in acid. Strategies for enhancing the stability of the Co_3O_4 in acid are essential in developing non-noble metal-based interfaces for OER. In addition, the Co_3O_4 tethered to ITO by SAM exhibits significantly higher Γ and higher TOF of the OER than the Co_3O_4 bound to ITO using Nafion, and we propose that evaluation of the nanoparticle electrocatalytic activities using Nafion as the binder in the electrode preparation would cause severe underestimation. Nevertheless, binding nanoparticle electrocatalysts with Nafion or other ionomers is currently the most practical way of fabricating the membrane electrode assembly in fuel cells and water electrolyzers. The nanoparticle-tethered electrodes are promising as platforms for evaluation of the electrochemical catalytic activities of the nanoparticles.

Data availability statement

The original contributions presented in the study are included in the article/Supplementary Material; further inquiries can be directed to the corresponding authors.

Author contributions

XL: Writing, revision, funding acquisition, and data analysis; QT: Experimental, data analysis, and writing; YL: Experimental and revision; ZZ: Experimental and data analysis; JW: Funding acquisition; SL: Funding acquisition and supervision; CW: Funding acquisition, writing, editing, revision, data analysis and supervision.

Funding

Acknowledgments

Conflict of interest

The authors declare that the research was conducted in the absence of any commercial or financial relationships that could be construed as a potential conflict of interest.

Publisher's note

All claims expressed in this article are solely those of the authors and do not necessarily represent those of their affiliated organizations, or those of the publisher, the editors, and the reviewers. Any product that may be evaluated in this article, or claim that may be made by its manufacturer, is not guaranteed or endorsed by the publisher.

Supplementary material

The Supplementary Material for this article can be found online at: https://www.frontiersin.org/articles/10.3389/fchem.2022.919192/full#supplementary-material

References

Anantharaj, S., Karthick, K., and Kundu, S. (2019). Spinel cobalt titanium binary oxide as an all-non-precious water oxidation electrocatalyst in acid. *Inorg. Chem.* 58, 8570–8576. doi:10.1021/acs.inorgchem.9b00868

Barfidokht, A., Ciampi, S., Luais, E., Darwish, N., and Gooding, J. J. (2013). Distance-dependent electron transfer at passivated electrodes decorated by gold nanoparticles. *Anal. Chem.* 85, 1073–1080. doi:10.1021/ac3029486

Canari, R., and Eyal, A. M. (2003). Effect of pH on dicarboxylic acids extraction by amine-based extractants. *Ind. Eng. Chem. Res.* 42, 1293–1300. doi:10.1021/ie010579p

Chazalviel, J.-N., and Allongue, P. (2011). On the origin of the efficient nanoparticle mediated electron transfer across a self-assembled monolayer. *J. Am. Chem. Soc.* 133, 762–764. doi:10.1021/ja109295x

Dong, Y., He, K., Yin, L., and Zhang, A. (2007). A facile route to controlled synthesis of Co_3O_4 nanoparticles and their environmental catalytic properties. *Nanotechnology* 18, 435602. doi:10.1088/0957-4484/18/43/435602

Dwivedi, N., Yeo, R., Satyanarayana, N., Kundu, S., Tripathy, S., and Bhatia, C. (2015). Understanding the role of nitrogen in plasma-assisted surface modification of magnetic recording media with and without ultrathin carbon overcoats. *Sci. Rep.* 5, 7772. doi:10.1038/srep07772

Gambardella, A. A., Feldberg, S. W., and Murray, R. W. (2012). Electron transfer dynamics of iridium oxide nanoparticles attached to electrodes by self-assembled monolayers. *J. Am. Chem. Soc.* 134, 5774–5777. doi:10.1021/ja301212r

Han, H., Kim, I., and Park, S. (2021). Thermally templated cobalt oxide nanobubbles on crumpled graphene sheets: A promising non-precious metal catalysts for acidic oxygen evolution. *Electrochimica Acta* 382, 138277. doi:10.1016/j.electacta.2021.138277

Hill, C. M., Kim, J., and Bard, A. J. (2015). Electrochemistry at a metal nanoparticle on a tunneling film: A steady-state model of current densities at a tunneling ultramicroelectrode. *J. Am. Chem. Soc.* 137, 11321–11326. doi:10.1021/jacs.5b04519

Hullar, T., and Anastasio, C. (2011). Yields of hydrogen peroxide from the reaction of hydroxyl radical with organic compounds in solution and ice. *Atmos. Chem. Phys.* 11, 7209–7222. doi:10.5194/acp-11-7209-2011

Huynh, M., Ozel, T., Liu, C., Lau, E. C., and Nocera, D. G. (2017). Design of template-stabilized active and earth-abundant oxygen evolution catalysts in acid. *Chem. Sci.* 8, 4779–4794. doi:10.1039/c7sc01239j

Kanicky, J. R., and Shah, D. O. (2002). Effect of degree, type, and position of unsaturation on the pKa of long-chain fatty acids. *J. Colloid Interface Sci.* 256, 201–207. doi:10.1006/jcis.2001.8009

Kellon, J. E., Young, S. L., and Hutchison, J. E. (2019). Engineering the nanoparticle–electrode interface. *Chem. Mat.* 31, 2685–2701. doi:10.1021/acs.chemmater.8b04977

Kizling, M., Dzwonek, M., Więckowska, A., and Bilewicz, R. (2018). Size does matter-mediation of electron transfer by gold clusters in bioelectrocatalysis. *ChemCatChem* 10, 1988–1992. doi:10.1002/cctc.201800032

Kollhoff, F., Schneider, J., Li, G., Barkaoui, S., Shen, W., Berger, T., et al. (2018). Anchoring of carboxyl-functionalized porphyrins on MgO, TiO_2, and Co_3O_4 nanoparticles. *Phys. Chem. Chem. Phys.* 20, 24858–24868. doi:10.1039/c8cp04873h

Lachmanová, Š. N., Vavrek, F., Sebechlebská, T., Kolivoška, V., Valášek, M., and Hromadová, M. (2021). Charge transfer in self-assembled monolayers of molecular conductors containing tripodal anchor and terpyridine-metal redox switching element. *Electrochimica Acta* 384, 138302. doi:10.1016/j.electacta.2021.138302

Lai, Q., Vediyappan, V., Aguey-Zinsou, K.-F., and Matsumoto, H. (2021). One-Step synthesis of carbon-protected Co_3O_4 nanoparticles toward long-term water oxidation in acidic media. *Adv. Energy Sustain. Res.* 2, 2100086. doi:10.1002/aesr.202100086

Lavagnini, I., Antiochia, R., and Magno, F. (2004). An extended method for the practical evaluation of the standard rate constant from cyclic voltammetric data. *Electroanalysis* 16, 505–506. doi:10.1002/elan.200302851

Liu, R., Shan, X., Wang, H., and Tao, N. (2019). Plasmonic measurement of electron transfer between a single metal nanoparticle and an electrode through a molecular layer. *J. Am. Chem. Soc.* 141, 11694–11699. doi:10.1021/jacs.9b05388

Liu, Z.-G., Chen, X., Liu, J.-H., and Huang, X.-J. (2013). Well-arranged porous Co_3O_4 microsheets for electrochemistry of Pb (II) revealed by stripping voltammetry. *Electrochem. Commun.* 30, 59–62. doi:10.1016/j.elecom.2013.02.002

Moghaddam, R. B., Wang, C., Sorge, J. B., Brett, M. J., and Bergens, S. H. (2015). Easily prepared, high activity Ir-Ni oxide catalysts for water oxidation. *Electrochem. Commun.* 60, 109–112. doi:10.1016/j.elecom.2015.08.015

Mondschein, J. S., Callejas, J. F., Read, C. G., Chen, J. Y., Holder, C. F., Badding, C. K., et al. (2017). Crystalline cobalt oxide films for sustained electrocatalytic oxygen evolution under strongly acidic conditions. *Chem. Mat.* 29, 950–957. doi:10.1021/acs.chemmater.6b02879

Mukerjee, P., and Ostrow, J. D. (2010). Review: Bilirubin pKa studies: New models and theories indicate high pKa values in water, dimethylformamide and DMSO. *BMC Biochem.* 11, 15. doi:10.1186/1471-2091-11-15

Natarajan, K., Munirathinam, E., and Yang, T. C. (2021). Operando investigation of structural and chemical origin of Co_3O_4 stability in acid under oxygen evolution reaction. *ACS Appl. Mater. Interfaces* 13, 27140–27148. doi:10.1021/acsami.1c07267

Shermukhamedov, S. A., Nazmutdinov, R. R., Zinkicheva, T. T., Bronshtein, M. D., Zhang, J., Mao, B., et al. (2020). Electronic spillover from a metallic nanoparticle: Can simple electrochemical electron transfer processes be catalyzed by electronic coupling of a molecular scale gold nanoparticle simultaneously to the redox molecule and the electrode? *J. Am. Chem. Soc.* 142, 10646–10658. doi:10.1021/jacs.9b09362

Shinagawa, T., Garcia-Esparza, A. T., and Takanabe, K. (2015). Insight on Tafel slopes from a microkinetic analysis of aqueous electrocatalysis for energy conversion. *Sci. Rep.* 5, 13801–13821. doi:10.1038/srep13801

Silva, B. P., de Florio, D. Z., and Brochsztain, S. (2014). Characterization of a perylenediimide self-assembled monolayer on indium tin oxide electrodes using electrochemical impedance spectroscopy. *J. Phys. Chem. C* 118, 4103–4112. doi:10.1021/jp409416b

Song, J., Wei, C., Huang, Z.-F., Liu, C., Zeng, L., Wang, X., et al. (2020). A review on fundamentals for designing oxygen evolution electrocatalysts. *Chem. Soc. Rev.* 49, 2196–2214. doi:10.1039/c9cs00607a

Srinivasa, N., Shreenivasa, L., Adarakatti, P. S., Crapnell, R. D., Rowley-Neale, S. J., Siddaramanna, A., et al. (2020). Functionalized Co_3O_4 graphitic nanoparticles: A high performance electrocatalyst for the oxygen evolution reaction. *Int. J. Hydrogen Energy* 45, 31380–31388. doi:10.1016/j.ijhydene.2020.08.231

Tian, Q., Chai, L., Zhou, Z., and Wang, C. (2021). Construction of iridium oxide nanoparticle modified indium tin oxide electrodes with polycarboxylic acids and pyrophosphoric acid and their application to water oxidation reactions. *Electrochimica Acta* 389, 138683. doi:10.1016/j.electacta.2021.138683

Walter, M. G., Warren, E. L., McKone, J. R., Boettcher, S. W., Mi, Q., Santori, E. A., et al. (2010). Solar water splitting cells. *Chem. Rev.* 110, 6446–6473. doi:10.1021/cr1002326

Wang, X., Colavita, P. E., Streifer, J. A., Butler, J. E., and Hamers, R. J. (2010). Photochemical grafting of alkenes onto carbon surfaces: Identifying the roles of electrons and holes. *J. Phys. Chem. C* 114, 4067–4074. doi:10.1021/jp911264n

Xiao, Z., Huang, Y.-C., Dong, C.-L., Xie, C., Liu, Z., Du, S., et al. (2020). Operando identification of the dynamic behavior of oxygen vacancy-rich Co_3O_4 for oxygen evolution reaction. *J. Am. Chem. Soc.* 142, 12087–12095. doi:10.1021/jacs.0c00257

Xie, C., Niu, Z., Kim, D., Li, M., and Yang, P. (2019). Surface and interface control in nanoparticle catalysis. *Chem. Rev.* 120, 1184–1249. doi:10.1021/acs.chemrev.9b00220

Yang, D., Velamakanni, A., Bozoklu, G., Park, S., Stoller, M., Piner, R. D., et al. (2009). Chemical analysis of graphene oxide films after heat and chemical treatments by X-ray photoelectron and Micro-Raman spectroscopy. *Carbon* 47, 145–152. doi:10.1016/j.carbon.2008.09.045

Young, S. L., Kellon, J. E., and Hutchison, J. E. (2016). Small gold nanoparticles interfaced to electrodes through molecular linkers: A platform to enhance electron transfer and increase electrochemically active surface area. *J. Am. Chem. Soc.* 138, 13975–13984. doi:10.1021/jacs.6b07674

Zhang, S.-Y., Li, T.-T., Zhu, H.-L., and Zheng, Y.-Q. (2018). Co_3O_4 polyhedrons with enhanced electric conductivity as efficient water oxidation electrocatalysts in alkaline medium. *J. Mat. Sci.* 53, 4323–4333. doi:10.1007/s10853-017-1855-2